Implementation of the toroidal absorption cell with multi-layer patterns by a single ring surface

Hong Chang,[1] Shiling Feng,[1] Xuanbing Qiu,[1] Huiyan Meng,[1] Guqing Guo,[1] Xiaohu He,[1] Qiusheng He,[1] Xiaohua Yang,[2] Weiguang Ma,[3] (iD) Ruifeng Kan,[4] Christa Fittschen,[5] and Chuanliang Li[1,*] (iD)

[1]*Department of Physics, Taiyuan University of Science and Technology, Taiyuan 030024, China*
[2]*School of Science, Nantong University, Nantong 226019, China*
[3]*State Key Laboratory of Quantum Optics and Quantum Optics Devices, Institute of Laser Spectroscopy, Shanxi University, Taiyuan 030006, China*
[4]*State Key Laboratory of Applied Optics, Changchun Institute of Optics, Fine Mechanics and Physics, Chinese Academy of Sciences, Changchun, Jilin 130033, China*
[5]*Université Lille, CNRS, UMR 8522—PC2A—Physicochimie des Processus de Combustion et de l'Atmosphère, Lille F-59000, France*
*Corresponding author: li_chuanliang@126.com

We developed a type of toroidal multi-pass cell with multi-layer patterns based on the off-axis model. The effective path length of the original toroidal multi-pass cell is extended several roundtrips in comparison with the single-layer pattern, since the inner surface of the toroidal multi-pass cell is more efficiently utilized. The light pattern has been achieved by using the simple ring surface, which is easy to fabricate. The exact analytical equations for the design of the toroidal multi-pass cell were derived based on analytical vector calculations. A series of numerical ray tracing simulations is presented, and the maximum theoretical optical path length that can be reached is 30 m with a setup of 5 cm column radius. Furthermore, two practical spot patterns are demonstrated with a path length of 8.3 m for a two-layer pattern and 10 m for a three-layer pattern, with respective effective volumes of 63 mL and 94 mL. Furthermore, the fringe effect is substantially reduced to less than 0.5% by the usage of our designed mask. © 2020 Optical Society of America

Multi-pass cells (MPCs) are extensively used in detecting trace compounds diluted in gaseous and liquid media because they allow increased sensitivity owing to their long optical path length (OPL). Several well-known MPCs, such as the Herriott cell [1–3], the White cell [4], and the Chernin cell [5,6], have been proposed and successfully used in spectroscopy to observe weak spectra of interest. Among these MPCs, the design of the Herriott cell has been continuously updated and improved because it commonly consists of two opposite mirrors and is susceptible to mechanical disturbance [7]. However, there is only a single eclipse pattern of reflection spots and most of the mirror area is not efficiently used in the Herriott cell, causing a limited OPL. As a result, perturbers based on astigmatic or cylindrical mirrors are employed to construct the Herriott cell

[8–10]. The number of light reflections in these modified cells is significantly increased and their spot distributions customarily exhibit a Lissajous-like pattern. Consequently, these cells increase the OPL and do not increase the spot overlap due to the more efficient utilization of the mirror area. Recently, several novel dense-pattern Herriott cells, even for spherical mirrors, were implemented by So and Thomazy [11], Liu *et al*. [12], Li *et al*. [13], and Dong *et al*. [14]. In 2019, Cue *et al*. investigated a Herriott cell with a dense spot pattern based on the spherical aberration, and they simulated a set of exotic spot patterns with highly efficient beam folding [15]. However, these cells require multiple parameters for fulfilling reentrant condition such as, distance, entrance angle, and tilt of the mirrors [16].

Recently, Bernacki [17], and Tuszon *et al*. [18] designed a compact toroidal multi-purpose distribution cable (MPC) with a low-volume monolithic ring. The OPL of the toroidal MPC can be flexibly changed solely by adjusting the entrance angle, and it is thus suitable for different absorption conditions of the sought-after species. In addition, it features mechanical robustness and is lightweight, which makes it attractive for building mobile and portable laser spectroscopy. Graf *et al*. [16] and Mangold *et al*. [19] used respectively paraboloid and emerging segmented inner surfaces to increase the number of reflections. We also proposed a spiral-torus structure cell for raising the number of reflections [20]. Recently, Yang *et al*. [21] designed a novel structure for a circular cell based on two spherical mirrors such that the heights and the position of two sphere centers are different. In addition, its maximum OPL is relevant to the positions of the entrance and exit holes. In practice, single spherical surfaces come with the advantage of high surface quality and low cost. Previous investigation of the toroidal cell focused on the number of reflections and numerical ray tracing modeling of a single-layer pattern [16,19–22]. To the best of our knowledge, the analytical method that is of significant importance for the

design of multi-layer patterns in a circular MPC has not been reported.

In this Letter, a new dense-pattern toroidal multi-pass cell with a ring surface and an absorption mask is proposed, whereby polygon star spot patterns can be generated on multiple layers of the inner surface of the toroidal cell due to off-axis irradiation. The prototype of the developed toroidal gold-coated absorption cell with the inner diameter of 100 mm and the outer diameter of 108 mm and the height of 20 mm is made of stainless steel. Its total mass is around 220 g. The design equations for exact analytical solutions to the toroidal cell are derived based on the analytical vector calculations; the astigmatism of our several designs is shown in the form of images. Two typical ray tracing simulations of two- and three-layer patterns are presented, and their corresponding practical experimental demonstrations with separately 8.3 m and 63 mL and 10 m and 94 mL are demonstrated.

The ABCD matrix is the simple mathematical form for ray tracing calculations at the condition of paraxial approximation. However, it cannot well describe the ray propagation of a circular cell because the paraxial theory ($\sin\theta \approx \theta$, where θ is the angle between incident ray and optical axis) may be invalid, and the direction of the optical axis rotates with reflections. The ray-tracing configuration is shown in Fig. 1(a). The M_0 (x_0, y_0, z_0) is the ray injection position and M_0' $(x_0', y_0', 0)$ is the projection of M_0 in the x-y plane. When the setup fulfills the stability conditions of a cavity, the beam is confined in the cell and travels back and forth. The stability condition is $L < 2R$ within the paraxial theory, and it has also been proved true in the circular cell by Yang *et al.* [22]. Herein, L is the separation distance of two mirrors and R is the radius of the curvature. The off-axis incident beam propagating in the cell results in reflections on different layers by the interior surface of the cell. Finally, the trajectory of light forms a polygon star at each layer and the beam exits the cell from the incident hole.

The geometric structure of a transmitting ray is shown in Fig. 1. Figures 1(a) and 1(b) are the stereogram and plan schematics. As shown in Fig. 1, the incident angle θ satisfies

$$\theta = \frac{\pi}{2} \cdot \left[1 - \frac{1+x}{m}\right], \qquad (1)$$

where x is the number of times the beam passes the x-axis and m is a nonzero number and is the number of spots per row.
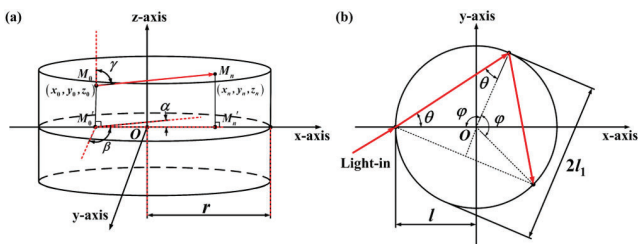
According to Eq. (1), we can derive all solutions of θ with various values of the x. For the case of $m = 5$, θ has two solutions of 18° and 54° and the values of x are 3 and 1. In our work, we need the long optical length; hence we present the following Eq. (2) for the unique solution that can calculate the longest optical length in all solutions of θ

$$\theta = \begin{cases} \frac{\pi}{2m}, & m = j \\ \frac{\pi}{m/2}, & m = 2j \\ \frac{\pi}{m}, & \text{otherwise,} \end{cases} \qquad (2)$$

where we assume j is an arbitrary positive odd number, such as, 1, 3, 5, 7, and so on. There are three cases for the values of m in Eq. (2). According to Eq. (2), we know that the value of θ depends on the multiple relationships between the values of m and j. For instance, for $m = 15$, θ is equal to 6°; if $m = 30$, the corresponding θ is 12°. For $m = 36$, according to case 3 and as a result, the value of θ is 5°. For the two-layer pattern, satisfying the closed path condition, m fulfills the following condition:

$$m = 4k + a, \qquad (3)$$

where $k \in N$ and the values of a are defined as 0, 1, 2, and 3. The analogous relationship for three-layer spot patterns is derived as follows:

$$m = 6k + a. \qquad (4)$$

Herein, the values of a are defined as 0, 1, 2, 3, 4, and 5.

In order to trace the trajectory of rays, we construct the vectors method to calculate each spot coordinate in the three-dimensional (3D) Cartesian system, as shown in Fig. 2. The two- and three-layer models are presented in Figs. 2(a) and 2(b), respectively. After n passes, the corresponding values of the rays could be expressed by the following equation:

$$d_n = \frac{x_n - x_{n-1}}{a_n} = \frac{y_n - y_{n-1}}{b_n} = \frac{z_n - z_{n-1}}{c_n}, \qquad (5)$$

where a_n, b_n, and c_n are the components of the direction vector along the respective x, y, and z axes at the nth pass. They are given as follows:

Fig. 1. (a) Propagation of the light rays from position M_0 (the incident point) to position M_n (after the nth pass) in the 3D rectangular coordinate system. M_0' and M_n' are the projections of the M_0 and M_n in the x-y plane; α, β and γ, are the three axial-twist angles between the incident ray and the three axes; r, the radius of curvature in the tangential direction in the x-y plane, which is equal to the cell radius. (b) Top view of the reflections. θ, the incident angle of the spot pattern in the x-y plane; O, the origin of the coordinate system; l, the horizontal distance between the spot and the z-axis; l_1, the distance after rotation to the z-axis in the normal direction.
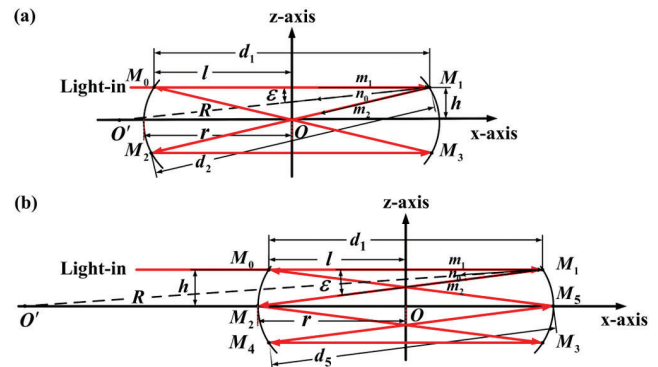

Fig. 2. Transmission of the rays in the x-z plane. $d_{1,2\_n}$, the pathlength of the 1, 2 ... nth pass count on the inner surface of the toroidal cell; h, the vertical distance of the entrance beam in the z-axis and equal to x_0; R, the sagittal curvature of the toroidal surfaces; O', the center of the circle with the radius of R; m_1, m_2, the vectors of the input beam and the reflected beam; n_0, the normal vector of the toroidal surface; ε, the angle between the vector m_1 and n_0. The distribution of the spots of the (a) two-layer and (b) three-layer on the toroidal mirror surface.

$$a_n = k_{1n} + a_{n-1}, \quad b_n = k_{2n} + b_{n-1}, \quad c_n = k_{3n} + c_{n-1}.$$
$$(6)$$

The variables with script $n-1$ represent the parameters at the $(n-1)$th pass count.

Likewise, k_{1n}, k_{2n}, and k_{3n} are the vectors of the normal vector n_0 along the x, y, and z axes, and their corresponding magnitudes (k_{1n}, k_{2n}, and k_{3n}) are

$$k_{1n} = -4 \cdot x_n \cdot \tau,$$

$$k_{2n} = -4 \cdot y_n \cdot \tau,$$

$$k_{3n} = 4 \cdot z_n \cdot \frac{\left(R - r - \sqrt{R^2 - z_n^2}\right)}{\sqrt{R^2 - z_n^2}} \cdot \tau,$$

where

$$\tau = \frac{2 \cdot a_n \cdot x_n + 2 \cdot b_n \cdot y_n + (-2) \cdot c_n \cdot z_n \cdot \frac{\left(R - r - \sqrt{R^2 - z_n^2}\right)}{\sqrt{R^2 - z_n^2}}}{4 \cdot x_n^2 + 4 \cdot y_n^2 + \left\{(-2) \cdot z_n \cdot \frac{\left(R - r - \sqrt{R^2 - z_n^2}\right)}{\sqrt{R^2 - z_n^2}}\right\}^2},$$
$$(7)$$

where a_n, b_n, and c_n are the corresponding magnitudes of a_n, b_n, and c_n, respectively. The values of a_n, b_n, and c_n, and their transitive relation can be calculated using the trigonometrical function. The expression of y_n is derived by substituting Eqs. (6) and (7) with Eq. (5)

$$y_n = -\frac{2 \cdot (\iota_1 + \iota_2)}{\left(\frac{a_n}{b_n}\right)^2 + \left(\frac{c_n}{b_n}\right)^2 + 1} - y_{n-1},$$

where

$$\iota_1 = \frac{a_n}{b_n} \cdot \left(x_{n-1} - y_{n-1} \cdot \frac{a_n}{b_n}\right),$$

$$\iota_2 = \frac{c_n}{b_n} \cdot \left(z_{n-1} - y_{n-1} \cdot \frac{c_n}{b_n}\right).$$
$$(8)$$

Then, it is straightforward to obtain the values of d_n, x_n, and z_n according to Eq. (5). Therefore, we can derive Eq. (9), which is about x_n and z_n

$$x_n = (y_n - y_{n-1}) \cdot \frac{a_n}{b_n} + x_{n-1}, \quad z_n = (y_n - y_{n-1}) \cdot \frac{c_n}{b_n} + z_{n-1}.$$
$$(9)$$

The desired OPL can be flexibly constructed by a pair of m and d_n by simply changing the incidence angle. In principle, the above expressions about the ray transmission can be used with a positive integer of spot-layers without taking into consideration the astigmatism.

Four examples, as plotted in Fig. 3, show the sequent propagation paths of the beam in the toroidal cell. In comparison with the single-layer parabolic circular mirror and the multi-layer spherical mirror, our cell possesses the characteristics of simpler structure, easier adjustment, simple manufacture, and flexibility. For clarity, the beam diameter and the distance between neighboring layers are equal for avoiding overlapping laser spots; the distance between spot layers in Figs. 3(a) and 3(b) is 4 mm, and the number of each layer reflection is set to 10. The OPLs in
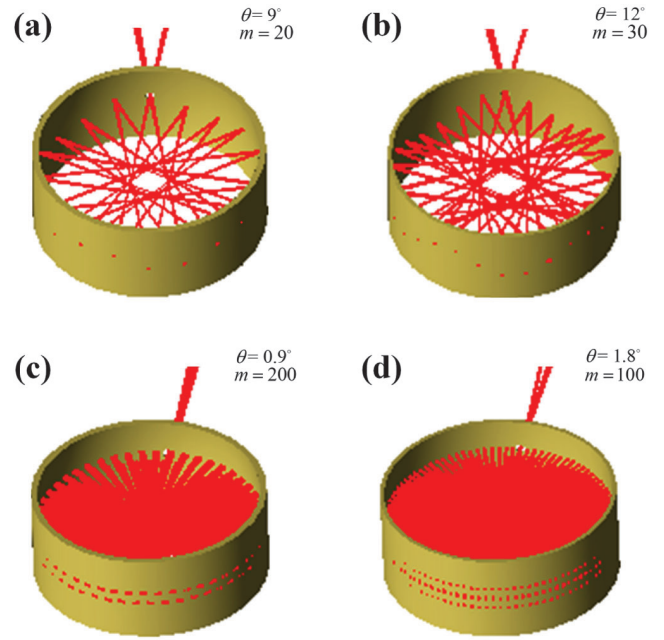

Fig. 3. (a) A two-layer example with 20 passes. (b) A three-layer example with 30 passes. (c) The largest number of reflections (200 times) among two-layer simulating cases with $r = 50$ mm, $R = 100$ mm, and 63 mL. (d) The largest number of reflections (300 times) among three-layer simulating cases with $r = 50$ mm, $R = 200$ mm, and 94 mL.

Figs. 3(c) and 3(d) are approximately 20 and 30 m, respectively. The ratios of OPL to volume is derived by dividing the OPL by the effective volume of the absorption cell. The effective volume of the cell is defined as $V = \pi r^2 h$. So in the case of a large number of reflections, the ratio of OPL to volume for the two- and three-layer patterns and for the single-layer ring cavity is equivalent to each other (32 cm^{-2}). However, the OPL is increased two and three times for two- and three-layer patterns in comparison with the coaxial single-layer pattern, respectively.

The calculated and practical spot patterns are exhibited in Fig. 4. Herein, a diode laser emitting at 635 nm and the absorption mask were employed to observe the practical spot patterns. Based on the simulation, a mask was designed and produced by a 3D printer to reduce the fringe effect. It includes a barrier and slits that distribute evenly in response to the beam pattern. In Figs. 4(a) and 4(b), the incident angle θ is adjusted, respectively, as 8.6° and 10.6° to achieve 84 passes and 102 passes. Therefore, the OPLs are 8.3 m and 10 m and their corresponding ratios are 13 and 11 cm^{-2}, respectively. The ratios of OPL to volume could be improved through minimizing the spot size to increase the maximum OPL by increasing the number of reflections. They could also be improved through reducing the volume of the cell by adding a cylinder into the empty volume of the center of the cell without blocking the beam.

The off-axis reflections may result in astigmatism, but the phenomenon is not serious for the two- and three-layer pattern, as depicted in the inserts of Fig. 4. The stray light from each reflection is blocked by the barriers of the mask and the intensity of the beam is decreased due to reflectivity. After several folds the beam is not clearly visible anymore, but the position of the mask slits is illuminated, as shown in Fig. 4. Therefore, it can be confirmed that the simulation and the experiment are consistent
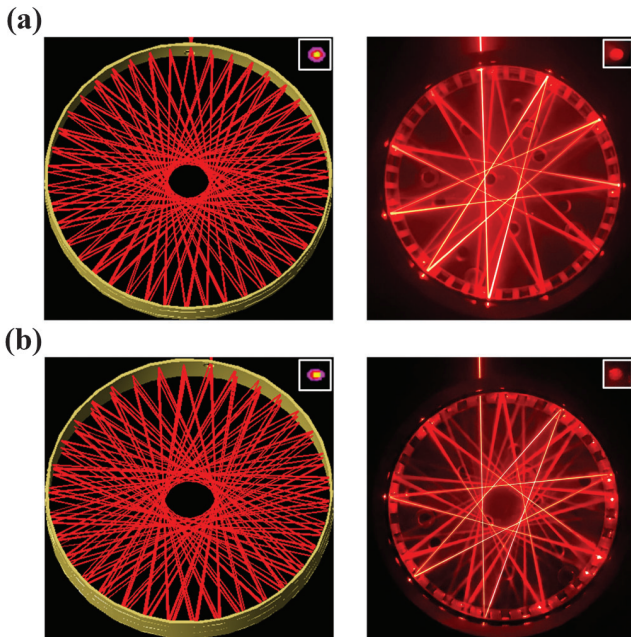
(a)

(b)

Fig. 4. Calculated (left) and practical (right) beam patterns and their light shapes of the output beam of (a) the two-layer and (b) the three-layer spot patterns. The inserts show the exit beam spot for each pattern.

and the astigmatism is negligible. Furthermore, the quality of the practical output beam profile is considerably improved when equipped with the designed mask.

Moreover, in order to verify the capability of the fringe suppression of the cell, we used the triangular wave signal with the frequency of 5 Hz generated by a signal generator to scan the laser frequency. The laser beam exiting from the cell is detected by a photo detector to obtain both the sine-similar interference signal and the scanning background. We defined the fringe-noise level as the amplitude ratio between the sine-similar and the triangular wave at its center. The etalon effect has been significantly suppressed in detection. For further validation, the baseline measurement results are shown in Fig. 5. The fringe-noise level of the two-layer and the three-layer spot patterns are 0.35% and 0.21%, respectively, comparable with the one-layer pattern of Ref. [23].

In summary, we reported the implementation of a multi-layer spot pattern in a toroidal multi-pass cell with a simple ring surface. The analytical equations for general solutions for the ray trajectory in the cell are obtained according to the analytical vector calculations. The monolithic nature of the cell and the

low volume guarantee robustness, rapid response, and simple adjustment. Two prototypes of practical use of the cell are demonstrated by adjusting different incident angles, resulting in an OPL of 8.3 m and 10 m with an effective volume of 63 mL and 94 mL, respectively. Due to highly efficient utilization of the inner surface, the fringe effects with the multi-layer pattern will be reduced compared to the single-layer pattern and are significantly declined to less than 0.5%. This makes this new design suitable for a variety of spectroscopic applications.

REFERENCES

1. D. Herriott, H. Kogelnik, and R. Kompfner, Appl. Opt. **3**, 523 (1964).
2. X. Guo, F. Zheng, C. Li, X. Yang, N. Li, S. Liu, J. Wei, X. Qiu, and Q. He, Opt. Lasers Eng. **115**, 243 (2019).
3. C. Li, L. Shao, H. Meng, J. Wei, X. Qiu, Q. He, W. Ma, L. Deng, and Y. Chen, Opt. Express **26**, 29330 (2018).
4. J. U. White, J. Opt. Soc. Am. **32**, 285 (1942).
5. Y. Wang, Z. Li, X. Liu, F. Fang, and X. Zhang, Appl. Opt. **56**, 8541 (2017).
6. S. M. Chernin, Spectrochim. Acta A **52**, 1009 (1996).
7. C. Robert, Appl. Opt. **46**, 5408 (2007).
8. D. R. Herriott and H. J. Schulte, Appl. Opt. **4**, 883 (1965).
9. J. Altmann, R. Baumgart, and C. Weitkamp, Appl. Opt. **20**, 995 (1981).
10. J. A. Silver, Appl. Opt. **44**, 6545 (2005).
11. S. So and D. Thomazy, "Multipass cell using spherical mirrors while achieving dense spot patterns," U.S. patent 8,531,659 B2 (10 September 2013).
12. K. Liu, L. Wang, T. Tan, G. Wang, W. Zhang, W. Chen, and X. Gao, Sens. Actuators B **220**, 1000 (2015).
13. C. Li, L. Dong, C. Zheng, and F. K. Tittel, Sens. Actuators B **232**, 188 (2016).
14. L. Dong, C. Li, N. P. Sanchez, A. K. Gluszek, R. J. Griffin, and F. K. Tittel, Appl. Phys. Lett. **108**, 011106 (2016).
15. R. Cui, L. Dong, H. Wu, S. Li, X. Yin, L. Zhang, W. Ma, W. Yin, and F. K. Tittel, Opt. Lett. **44**, 1108 (2019).
16. M. Graf, L. Emmenegger, and B. Tuzson, Opt. Lett. **43**, 2434 (2018).
17. B. Bernacki, "Multipass optical device and process for gas and analyte determination," U.S. patent 7,876,443 B2 (25 January 2011).
18. B. Tuzson, M. Mangold, H. Looser, A. Manninen, and L. Emmenegger, Opt. Lett. **38**, 257 (2013).
19. M. Mangold, B. Tuzson, M. Hundt, J. Jágerská, H. Looser, and L. Emmenegger, J. Opt. Soc. Am. A **33**, 913 (2016).
20. F. Wu, C. Li, W. Shi, J. Wei, and L. Deng, Spectrosc. Spectr. Anal. **36**, 1051 (2016).
21. Z. Yang, M. Zou, and L. Sun, Opt. Express **27**, 32883 (2019).
22. Z. Yang, Y. Guo, X. Ming, and L. Sun, Sensors **18**, 2680 (2018).
23. M. Graf, H. Looser, L. Emmenegger, and B. Tuzson, Opt. Lett. **42**, 3137 (2017).
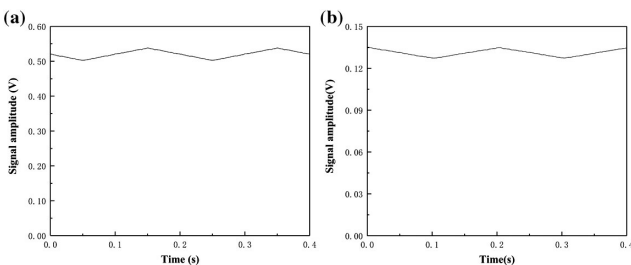
(a)

(b)

Fig. 5. Baseline measurement of the output beam of (a) the two-layer and (b) the three-layer spot patterns corresponding to the inserts of Figs. 4(a) and 4(b).